







## Effect of rainfall on a colluvial landslide in a debris flow valley


**QIAO Liang**<sup>1</sup>  <http://orcid.org/0000-0002-6599-3627>; e-mail: qiaoliang19881988@163.com


**MENG Xing-min**<sup>1\*</sup>  <http://orcid.org/0000-0002-3644-4899>;  e-mail: xmmeng@lzu.edu.cn

**CHEN Guan**<sup>1</sup>  <http://orcid.org/0000-0001-8834-039X>; e-mail: gchen@lzu.edu.cn

**ZHANG Yi**<sup>1</sup>  <http://orcid.org/0000-0001-7105-9497>; e-mail: zhangyi2013@lzu.edu.cn

**GUO Peng**<sup>1</sup>  <http://orcid.org/0000-0003-4093-0790>; e-mail: guopeng.lzu@gmail.com

**ZENG Run-qiang**<sup>1</sup>  <http://orcid.org/0000-0002-4554-8913>; e-mail: zengrunqiang@gmail.com

**LI Ya-jun**<sup>2</sup>  <http://orcid.org/0000-0002-3167-9330>; e-mail: lyjun10@gmail.com

\* Corresponding author

<sup>1</sup> Key Laboratory of Western China's Environmental Systems (Ministry of Education), Lanzhou University, Lanzhou 730000, China

<sup>2</sup> Geography Department, Royal Holloway, University of London, Surrey TW20 0EX, UK

**Citation:** Qiao L, Meng XM, Chen G, et al. (2017) Effect of rainfall on a colluvial landslide in a debris flow valley. Journal of Mountain Science 14(6). DOI: 10.1007/s11629-016-4142-9

© Science Press and Institute of Mountain Hazards and Environment, CAS and Springer-Verlag Berlin Heidelberg 2017

**Abstract:** A colluvial landslide in a debris flow valley is a typical phenomena and is easily influenced by rainfall. The direct destructiveness of this kind of landslide is small, however, if failure occurs the resulting blocking of the channel may lead to a series of magnified secondary hazards. For this reason it is important to investigate the potential response of this type of landslide to rainfall. In the present paper, the Goulingping landslide, one of the colluvial landslides in the Goulingping valley in the middle of the Bailong River catchment in Gansu Province, China, was chosen for the study. Electrical Resistivity Tomography (ERT), Terrestrial Laser Scanning (TLS), together with traditional monitoring methods, were used to monitor changes in water content and the deformation of the landslide caused by rainfall. ERT was used to detect changes in soil water content induced by rainfall. The most significant findings were as follows:(1) the water content in the central-upper part (0~41 m) of the landslide was greater

than in the central-front part (41~84 m) and (2) there was a relatively high resistivity zone at depth within the sliding zone. The deformation characteristics at the surface of the landslide were monitored by TLS and the results revealed that rainstorms caused three types of deformation and failure: (1) gully erosion at the slope surface; (2) shallow sliding failure; (3) and slope foot erosion. Subsequent monitoring of continuous changes in pore-water pressure, soil pressure and displacement (using traditional methods) indicated that long duration light rainfall (average 2.22 mm/d) caused the entire landslide to enter a state of creeping deformation at the beginning of the rainy season. Shear-induced dilation occurred for the fast sliding (30.09 mm/d) during the critical failure sub-phase (EF). Pore-water pressure in the sliding zone was affected by rainfall. In addition, the sliding L1 parts of the landslide exerted a discontinuous pressure on the L2 part. Through the monitoring and analysis, we conclude that this kind of landslide may have large deformation at the beginning and the late of the rainy season.

**Received:** 27 July 2016

**Revised:** 5 January 2017

**Accepted:** 16 January 2017

**Keywords:** Colluvial landslide; Debris flow; Rainfall; Electrical resistivity tomography; Terrestrial laser scanning; Electrical resistivity tomography

**Notation:**

$\tau$	Shear stress in the sliding zone
$c$	Soil cohesion in the sliding zone
$\varphi$	Internal friction angle in the sliding zone
$\sigma$	Total normal stress in the sliding zone
$\mu$	Pore-water pressure in the sliding zone
$m$	Landslide mass per unit area in the sliding surface
$a$	Landslide acceleration
$t_{def}$	Time scale for deformation of the sliding zone
$t_{diff}$	Time scale for pore-water pressure diffusion
$K$	Hydraulic conductivity of the sliding zone
$E$	Young's modulus of the sliding zone
$\gamma_w$	Unit weight of water
$T$	Thickness of the landslide
$v$	Velocity

## Introduction

A colluvial landslide is a landslide body composed of colluvial deposits which usually rest on a bedrock surface. Colluvial deposits are generally loose, unconsolidated sediments ranging from silt to rock fragments of various sizes (e.g., Song and Cui 2015; Lacerda 2007; Meisina and Scarabelli 2007). Colluvial landslides are a significant hazard in many parts of the world, especially in mountainous areas in tropical and subtropical regions (e.g., Baum et al. 1993; Ochiai et al. 2004; Meisina and Scarabelli 2007). It is generally accepted that rainfall is one of the most important triggering factors, and therefore understanding the behavior of colluvial soils under rainfall conditions is essential for predicting colluvial landslides.

So far, there have been two principal approaches adopted in the study of colluvial landslides induced by rainfall. One approach is the study of the critical thresholds, which usually include antecedent rainfall, rainfall intensity, rainfall duration and soil water content, and the analysis of the relationship between the movement of the colluvial landslide and rainfall (e.g., Polemio et al. 1999; Crozier 1999; Dai et al. 2001; Aleotti 2004; Giannecchini 2006; Guzzetti et al. 2007; Bai et al. 2010). The other approach is to study the mechanism of landslide instability based on current theories of the nature of the failure

mechanism. This is usually conducted by monitoring parameters such as soil water content, pore water pressure, matrix suction, earth pressure and groundwater (e.g., Anderson and Sitar 1995; Tsaparas et al. 2002; Ochiai et al. 2004; Chen et al. 2003; Tu et al. 2009; Chen 2014).

During the rainy season, this kind of landslide may block the channel and forms a barrier lake. If the barrier dam fails, huge debris flows may occur, and if they are large enough, the sediments may block the Bailong river. This occurred in the case of the Zhouqu debris flow (Wang 2013), so it is significant to study the deformation of colluvial landslides under rainfall. The Goulingping landslide (Figure 1) is only one of thousands of colluvial landslides within the Bailong catchment in Gansu Province, North China. According to the records, the landslide has blocked the valley channel 4 times which magnified the effect of debris flows and destroyed more land and roads than usual. In this paper, three methods were used to monitor changes in soil water content and landslide deformation. Under conditions of natural rainfall, infiltration-induced variations in soil water content of the landslide were monitored by Electrical Resistivity Tomography (ERT). In addition, variations in surface deformation of the landslide triggered by rainstorms were monitored by Terrestrial Laser Scanning (TLS). Subsequently, displacement, pore-water pressure, soil pressure and the amount of rainfall were measured using traditional instrumentation (displacement meter, piezometer, earth pressure cell, and rain gauge).

## 1 Methods

Affected by M7 Wudu earthquake in 186 B.C. (Yuan et al. 2007) and Zhouqu - Bailongjiang Fault (Figure 1b), there are a lot of deposits along Goulingping valley. And the Goulingping landslide (Figure 1a) is one and located in basin in the middle of the Bailong River catchment, about 2 km from the mouth and on the right, concave, side. To the right of the landslide there is a debris flow terrace with a height of ~115 m and with farmland on the top. The debris flow deposits are mainly rudstone, which consists of fine-grained, abrasive particulate material. On the left side, (Figure 1b), the deposits consist solely of strongly weathered phyllite. The attitude of the unweathered phyllite

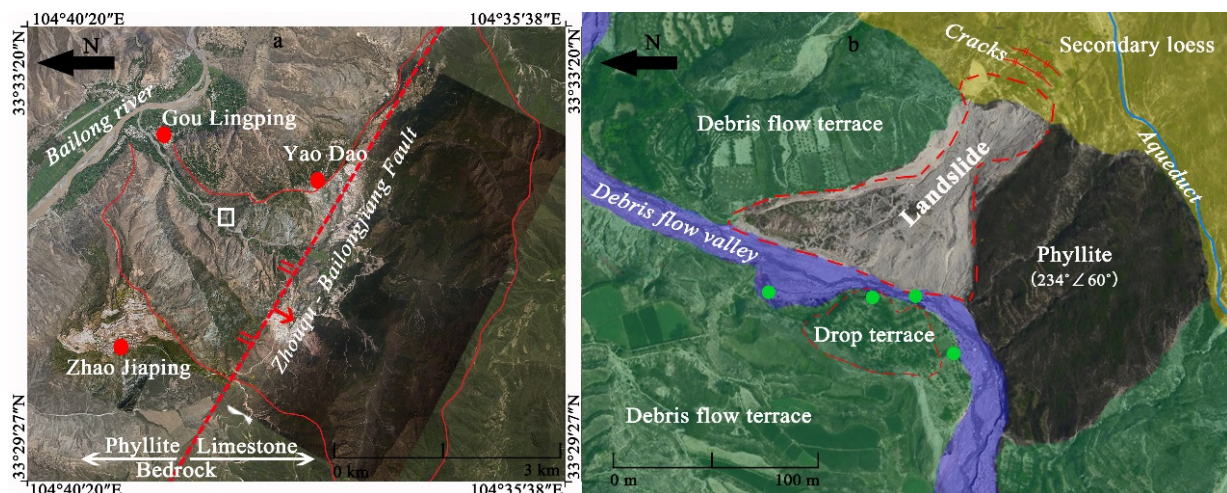


**Figure 1** The colluvial Goulingping landslide (33°31'46"N, 104°38'28"E). Green dots are the monitoring sites and the red dots are villages. Inset map shows the location of the study area in China.

underneath the weathering crust is  $234^{\circ} \angle 60^{\circ}$  and the slope angle exceeds  $70^{\circ}$ . Above the landslide the deposits consist of re-deposited loess and the slope angle is  $35^{\circ} \sim 60^{\circ}$ . Intense rainfall events and gully erosion caused the Goulingping landslide to fail and three monitoring technologies were chosen based on the depositional environment.

### 1.1 Electrical resistivity tomography (ERT)

Electrical Resistivity Tomography (ERT) has been increasingly applied to landslide investigations (e.g., Jongmans and Garambois 2007; Burda et al. 2013). Information about underground conditions is obtained by measuring changes in electrical resistivity, which often correspond to the boundaries between different layers. Electrical resistivity reflects the mineralogy of the soil particles, water content, porosity and the intrinsic matrix resistivity, and it varies with the degree of weathering and alteration in the space and time domains (e.g., Park and Kim 2005; Bievre et al. 2012). Some of these factors, such as an increase in soil water content and the consequent increase in pore water pressure, can play an important role in triggering a landslide (e.g., Bishop 1960; Morgenstern and Price 1965). In addition, continuous monitoring of resistivity can provide information on the dynamic behavior of the slope, such as changes in the sliding belt and infiltration paths (e.g., Perrone et al. 2014; Chen 2014).

The AGI SuperSting 8-channel Resistivity Instrument was used to monitor changes in soil

resistivity. The inversion software used was EarthImager 2D. Forty-three electrodes were arranged in a 2-m spacing along profile AB (84 m, Figure 2b). The monitoring dates were 2014/7/17, 2014/10/30, and 2015/3/26. These dates corresponded to the middle, late and early parts of the rainy season, respectively. In addition, changes in soil water content and soil density, and the sliding zone and infiltration path, were measured during different rainfall periods.

### 1.2 Terrestrial laser scanning (TLS)

Terrestrial laser scanning (TLS) is a recently-developed surveying technique which is being increasingly used to monitor landslide deformation (e.g., Teza et al. 2007; Monserrat and Crosetto 2008; Casula et al. 2010). TLS generates point clouds with each point being determined by its location in three-dimensional space and the intensity of the reflected signal. The data set can be used to generate a best-fit surface over the entire study area, and ground deformation can be identified using two or more ground surface models derived from TLS (Wang et al. 2011).

In the present research, monitoring was carried out using a Riegl LPM-321 Long Range Scanner which provides a single point accuracy of 25 mm at 50 m + 20 ppm and a measurement rate of 1000 points/s. In order to scan the entire landslide, four scan stations (Figure 1, green points) were established, and the point clouds from the neighboring scan stations were automatically registered to create an integrated model during



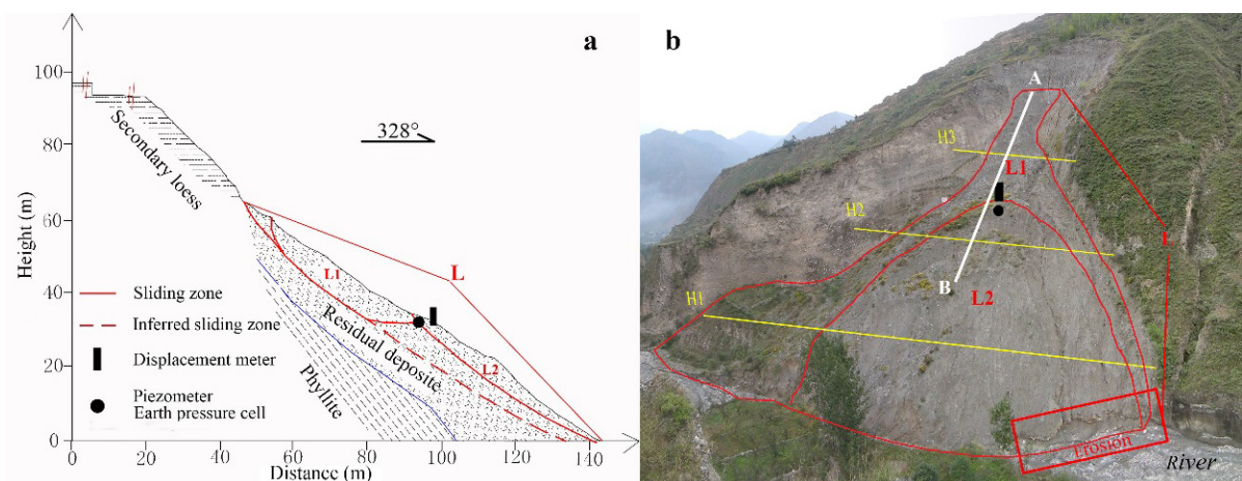


**Figure 2** Cross sectional view (with locations of the displacement meter, piezometer and earth pressure cell (a) and photograph (b) of the Goulingsping landslide.

each scanning. Nine scans were conducted from 2012-2013. The scanning resolution was 2 mm × 2 mm at a distance of 10 m, and the measurements were all made within a common coordinate system. The digital terrain models for each period were compared to assess changes in the deformation at the surface of the landslide during the two-year study interval. Daily rainfall was recorded at the same time using a rainfall gauge.

### 1.3 Others monitoring sensors

The monitoring instruments were initially installed in July 2014. They included a displacement meter, piezometer, earth pressure cell and rain gauge, and were used to measure displacement, pore-water pressure, soil pressure and the amount of rainfall at different locations. Prior to their installation in the field, all of the instruments were carefully checked in the laboratory and in addition the piezometer was calibrated. Details of the instruments used are given below.

*Displacement meter* -The model used was a BGK-3427 (Geokon, Beijing). The designed range is 4000 mm. One end of the displacement meter was installed in a stable location (the monitoring station) and the other end was installed in the upper part of L1 (Figure 2b).

*Piezometer*- ABGK-4500 standard piezometer (Geokon, Beijing) was used to measure in situ pore water pressure. This model is designed for low-pressure ranges, with a maximum of 7 kPa (±0.01 kPa accuracy), and thermistors are included to measure temperature. The instrument was

installed at a depth of 2 m beneath the sliding zone in the middle of the landslide (Figure 2b). The depth of 2 m was chosen based on the results of an earlier investigation.

*Earth pressure cell* - A standard earth pressure cell (BGK-4800S) was used to monitor soil pressure. The instrument can measure pressures up to 1 kPa (±0.01 kPa accuracy). The earth pressure cell was installed at a depth of 2.2 m within the sliding zone, perpendicular to the main direction of movement of the landslide. The main purpose of the instrument was to measure changes in the pressure exerted by the upper part of the landslide (L1) on the lower part (L2).

*Rain gauge*- A YM-04 tipping-bucket rain gauge, with a resolution of 0.2 mm, was installed to record the amount of rainfall. The gauge was installed in a stable part of the hillside, away from the landslide.

## 2 Results

The landslide we studied is 172 m in length (including the terrace at the rear of the landslide with several cracks), and 62 m in width. The main direction of landslide movement is about 328°, and the slope angle is 47°~51°. The landslide body is composed of strongly weathered phyllite fragments, secondary loess, and there is a small amount of limestone fragments at the surface (Figure 2a). Some Soil parameters are listed in Table 1. The average density of the landslide material is 2.0 g/cm<sup>3</sup>, and the liquid limit and plastic limit are 21%

and 15%, respectively. Under conditions of natural water content (13%), the soil cohesive force is 25 kPa and the internal friction angle is 30°. In in-situ and laboratory permeability experiment, the saturated infiltration rates of the landslide body and the sliding zone are about  $4.2 \times 10^{-6}$  m/s and  $9.2 \times 10^{-10}$  m/s, respectively. The thickness of the main landslide body (L) is about 15 m and it can be divided into two parts, L1 and L2 (Figure 2a).

**2.1 ERT measurements**

Based on the findings from an exploratory excavated pit it was found that the landslide material was composed of a mixture of relatively uniform weathered phyllite debris. Therefore, the resistivity distribution mainly reflects differences in soil water content and soil density. The three ERT images (Figure 3) reflect variations in soil water content in the middle, late and early parts of the rainy season, respectively. Based on the images, the distribution of the soil water content in the landslide body is complex; however, the following generalizations can be made.

According to the field survey, the landslide can be divided into two parts, L1 (0 ~ 60 m) and L2 (60 ~ 84 m). In L1, there is an obvious resistivity contrast between a relatively low resistivity zone (0 ~ 41 m) and a relatively high resistivity zone (41 ~ 60 m). Comparison of the three resistivity images reveals that the soil water content is layered

horizontally caused by the multiple advances of the wetting front during the monitoring period. The images also reveal that the soil water content progressively increased in the wet season and subsequently decreased gradually. In the middle part of L1 (10 ~ 41 m), the presence of loose soil at the surface is indicated by a relatively high resistivity zone and thus this part was likely to be prone to frequent sliding (Figure 3a). The rearrangement of soil particles induced by consolidation of the main sliding zone (at about 15-m depth; Figure 3b) reduced both the porosity and the permeability and in addition the presence of a static water layer formed above the main sliding zone reduced the soil strength (Figure 3c).

A relatively low-resistivity zone (Figure 3d) is present beneath the main sliding zone, indicating

**Table 1** Soil parameters and test methods

Soil parameters	Value	Method
Average density	2.0 g/cm <sup>3</sup>	Pycnometer test
Liquid limit	21%	Liquid-plastic limit combined test
Plastic limit	15%	
Natural water content	13%	Oven drying method
Cohesive force (13%)	25 kPa	Ring shear
Internal friction angle (13%)	30°	
Saturated infiltration rate	$4.2 \times 10^{-6}$ m/s (slide body)	In-situ permeability experiment
	$9.2 \times 10^{-10}$ m/s (slip zone)	Laboratory permeability experiment

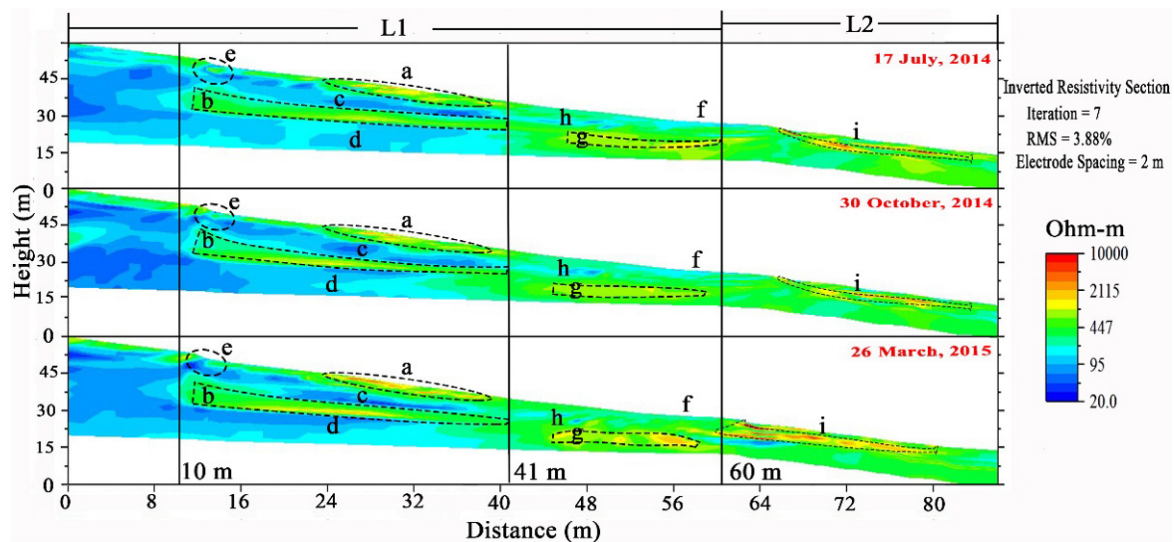


**Figure 3**ERT (Electrical Resistivity Tomography) images for 17 July, 2014; 30 October, 2014; and 26, March, 2015. The three dates correspond to the middle, late and early parts of the rainy season, respectively. Dotted lines indicate areas of contrast and the solid lines define various segments of the profile.

that the sliding zone was subject to some degree of water infiltration. In particular, the rear part of L1 was potentially prone to sliding since there was a well-developed crack (Figure 3e) which enabled the downward penetration of rainfall. In addition, the soil water content at the front of L1 (41 ~ 60 m) was lower than that in the middle-upper part due to compression and the fact that static water was prone to occur on the surface (Figure 3f) during rainstorms. The main sliding zone (~10 m depth in Figure 3g) also had a minor influence on the vertical distribution of soil water (Figure 3h).

The frequent sliding of L2 (60 ~ 84 m) clearly indicates that the main sliding zone is a relatively high resistivity zone (~5 m depth in Figure 3i) and that the sliding zone extends continuously upslope. Any sliding of L1 will exert a positive pressure on L2.

### 2.2 TLS measurements

We scanned the landslide a total of 9 times between 2012/1/15 and 2014/1/15 (S1-S9 in Figure 4). During this interval the total precipitation was 991 mm, with an average daily rainfall of 1.36 mm. In addition, there were 10 major rainstorm events (defined as those with a magnitude  $\geq 20$  mm/d). The scanning can be divided into two stages, namely in 2012 and 2013 (Figure 4). Total and average daily rainfall in 2012 were 502 mm and 1.37 mm, respectively; and the corresponding amounts for 2013 were 489 mm and 1.34 mm. Thus 2012 was somewhat wetter than 2013; however, the same number of rainstorm events (5) occurred in both years.

In the deformation plots derived from the TLS measurements (Figure 5), red represents accumulation, green represents no change, and blue represents erosion. All of the observed deformation occurred within the landslide and no

deformation occurred in the two side walls of the landslide.

Between 2012/5/3 and 2012/5/12 (Figure 5, S1-S2), there was erosion to a maximum depth of 7.72 m and accumulation to a maximum depth of 4.59 m; there was also large-scale deformation. During this interval, field observations revealed that a continuous and deep crack formed in the middle-rear part of the landslide. After two rainstorms (44.0 mm/d and 56.2 mm/d; Figure 4), rapid infiltration along the cracks not only increased the hydrostatic pressure and the soil weight, but also decreased the soil shear strength, causing large-scale deformation (Fan 2008). From 2015/5/ to 2013/5/13 (Figure 5, S2-S3), erosion occurred on the left side of the landslide and significant accumulation occurred in the middle-front part. The maximum erosion and accumulation depths were 3.72m and 4.41 m, respectively. The accumulation on the right side of the landslide was the result of the collapse of the steep hill.

From 2013/3/18 to 2013/4/18 (Figure 5, S3-S4), erosion to a maximum depth of 4.37 m occurred in the middle-left part of the landslide. This was caused by overland flow which washed out the loose soil in the unloading zone. From 2013/4/21 onwards, the toe of the landslide was frequently washed out by debris flows occurring during rainstorms which caused the continuous sliding of the front part of the landslide. From 2013/4/21 to 2013/7/6 (Figure 5, S4-S5), the erosion first occurred in the left-front part of the landslide and the displacement was 1.91 m; the height of the free face was 1.45 m and the length was 29.8 m. Between 2013/7/6 and 2013/7/17 (Figure 5, S5-S6), the front part of the landslide continued to slip, resulting in a displacement of 0.49 m and a free face length of 23.12 m.

In S6-S7, S7-S8 and S8-S9 (Figure 5), the

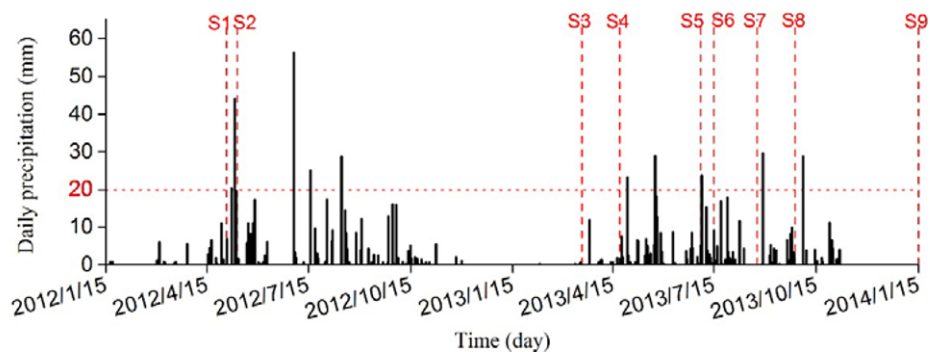


Figure 4 Daily rainfall and TLS (Terrestrial Laser Scanning) scanning dates.



deformation was relatively small and the toe of the landslide was the main deformation zone of the landslide; however, the free face became increasingly large, causing a reduction in slope stability.

Reference to the main longitudinal profile (Figure 6, left) shows that large-scale sliding occurred in the middle-rear part of the landslide and that accumulation occurred at the front. As a result of channel erosion, the front part of the landslide was frequently subject to sliding. The changes in the transverse profile (Figure 6, right) indicate that large-scale deformation mainly occurred at the rear, minor deformation occurred in the middle on both sides, and that frequent sliding occurred in the middle and left part of the front of the landslide. The landslide is located in the right and concave side of the valley and the left-front part of the landslide was directly affected by water erosion which is the reason for

the significant deformation at this location (Figure 1a).

### 2.3 Effect of rainfall on the landslide in 2015

The total and average daily rainfall in 2015 (661.7 mm and 2.6 mm, respectively) was much higher than in 2012 and 2013 (Figure 4 and Figure 7). In Figure 7, the minor fluctuations of the pore-water pressure curve and the soil pressure curve indicate that both responded rapidly to rainfall. For example, with the cessation of rainfall, pore-water pressure and soil pressure decreased significantly due to the dissipation and evaporation of water; and with the commencement of rainfall both parameters exhibit an obvious rise (Figure 7, Q). Therefore, soil pressure and pore water pressure can serve as sensitive indicators of the response of the landslide to rainfall. However, it is noteworthy that the displacement is also an important

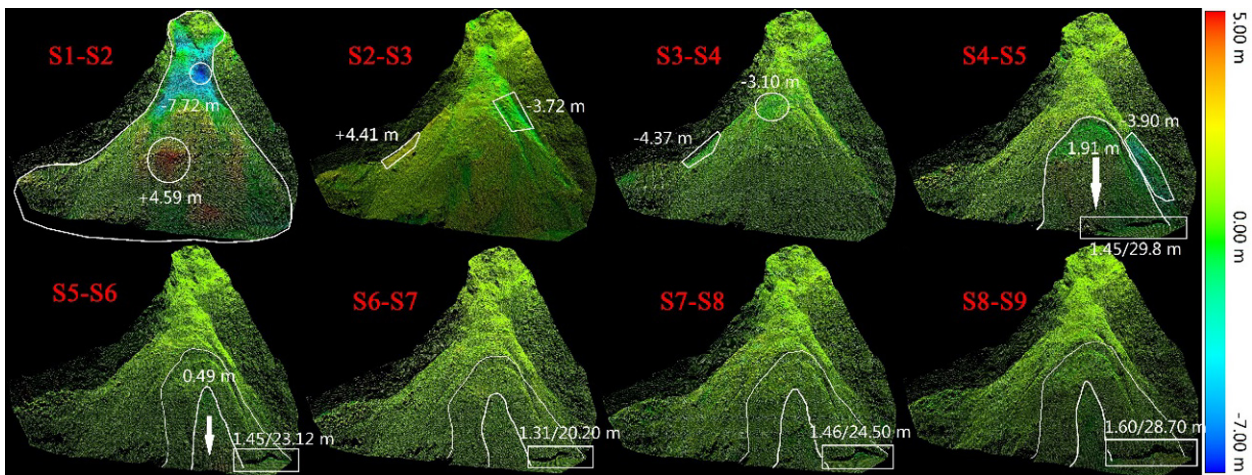


**Figure 5** Deformation of the landslide revealed by TLS measurements. Red represents accumulation, green represents no change, and blue represents erosion. +/- indicates accumulation (e.g. +4.59 m indicates an accumulation depth of 4.59 m). 1.45/23.12 m indicates a free face height of 1.45 m and a free face length of 23.12 m, etc.

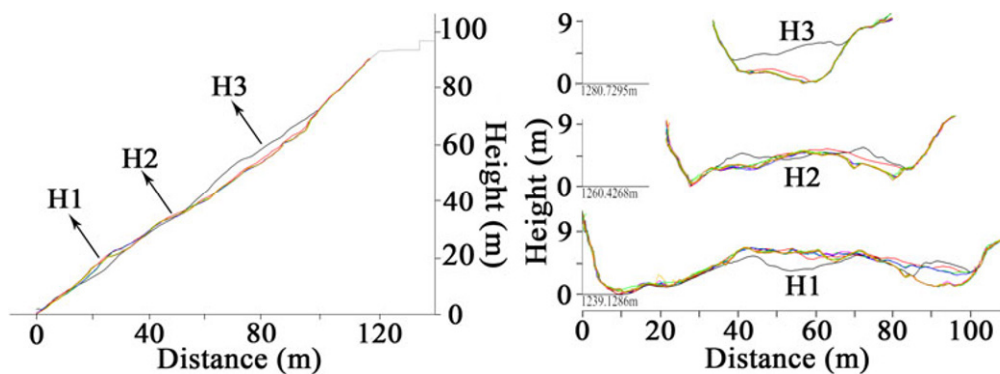


**Figure 6** Longitudinal (left) and transverse (right) profiles of the Goulingping landslide (the different colored curves represent profiles measured at different times).

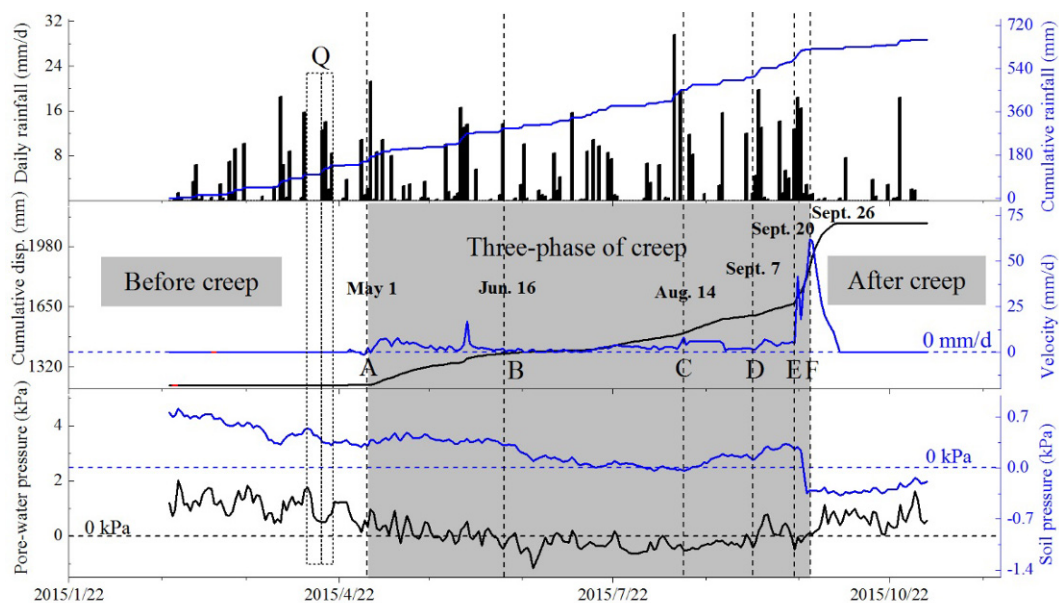


**Figure 7** Results of measurements of pore-water pressure, soil pressure and displacement (AB: Primary creep; BC: Secondary creep; CD: Initial accelerated sub-phase; DE: Intermediate accelerated sub-phase; EF: Critical failure sub-phase).

indicator of the landslide to rainfall. The accumulated displacement curve is consistent with the three-stage creep law proposed by Satio (1969). According to the classification proposed by Xu et al. (2011), the cumulative displacement can be divided into three phases: primary creep, secondary creep and tertiary creep. In addition, tertiary creep can be further divided into three sub-phases: initial acceleration, medium acceleration, and critical failure (Figure 7). In the different periods, the changes and reasons of three monitoring indexes were analysis combined with rainfall. In order to better interpret the responses to rainfall, average values of daily rainfall, displacement, pore-water pressure, soil pressure were calculated (Table 2).

In the early part of the rainy season prior to the initiation of creep, the increasing pore water pressure caused by the continuous rainfall (average 2.22 mm/d) reduced the effective stress in the soil. At the same time the pore water pressure (average of 1.1 kPa) reduced the soil shear strength in the static water layer around the sliding zone, causing the landslide to begin to creep. Before creep, the decrease reason of the soil pressure was that rainwater eroded the loose soil at the surface of L1 and the push of from L1 on L2 decreased.

During the primary creep phase (AB), the velocity was average 3.7 mm/d and the velocity was changing with time. At the beginning, the velocity

was about 5.2 mm/d and the velocity becomes more and more small. As the time, the value of the soil pressure was about 0.39 kPa without large change which indicated that L1 and L2 slide with the similar velocity. But the pore-water pressure gradually decreases to 0 kPa.

**Table 2** Average values of daily rainfall (Avg.-R), displacement (Avg.-D), pore-water pressure (Avg.-P), and soil pressure (Avg.-S) for different phases of landslide creep

Different phases	Avg.-R (mm/d)	Avg.-D (mm/d)	Avg.-P (kPa)	Avg.-S (kPa)
Before creep	2.22	0	1.1	0.52
AB	3.03	3.7	0.18	0.39
BC	2.74	1.75	-0.33	0.1
CD	2.21	4.39	-0.31	0.1
DE	4.86	4.55	0.23	0.25
EF	8.77	30.09	-0.11	0.06

**Notes:** AB: Primary creep; BC: Secondary creep; CD: Initial accelerated sub-phase; DE: Intermediate accelerated sub-phase; EF: Critical failure sub-phase.

In the secondary creep phase (BC), the velocity had not large change and about 1.75 mm/d and the pore-water pressure had small fluctuations around -0.33 kPa. And the soil pressure was more and more small from 0.38 kPa to 0 kPa which meant the velocity of L2 was large than L1's.

In the initial accelerated sub-phase (CD), compared with rainfall (average 2.21 mm/d), pore-water pressure (-0.31), the increasing pressure



(Figure 7, CD of the soil pressure curve) exerted by L1 on L2 part may have been the cause of the rate of sliding to increase to average 4.39 mm/d. As a result, the landslide entered the intermediate accelerated sub-phase (DE). Heavy rainfall (average of 4.86 mm/d) increased the pore-water pressure from average values of -0.31 kPa to 0.23 kPa, and the rate of sliding decreased to an average of 4.55 mm/d.

During the critical failure sub-phase (EF), rainstorms (average 8.77 mm/d) resulted in rapid sliding (average of 30.09 mm/d) and shrinkage of the soil mass in the sliding zone occurred which caused a decrease of the pore water pressure from 0.23 kPa to -0.11 kPa. Finally, the landslide failed. After the failure, the landslide attained a new steady state with the effective stress recovering and pore-water pressure returning to about 0.5 kPa.

### 3 Discussions and Conclusions

Based on the monitoring data, it is clear that the landslide was subject to deformation and that the main factor triggering instability was rainfall. As a result of rainfall events, the water content of the landslide varied systematically in time and space. The infiltration rate tracked seasonal variations in rainfall, which was the result of advances of the wetting front during the rainy season and retreats during the dry season. For the sliding of the landslide, the central-upper part (0 ~ 41 m) was under tension and the central-front part (41 ~ 84 m) was under compression. This promoted the greater development of fracturing in the central-upper part of the landslide than in the central-front zone, and therefore the amplitude of variation of the water content was greater in the former. In addition, the infiltration rate and water content in the sliding zone were relatively low.

Rainfall not only caused changes in soil water content, but also triggered variations in the degree of deformation. According to the analysis of the rainfall data and the field survey results, the duration of rainstorms was brief, normally only ~10 hours. In addition, rainstorm events of magnitude >20 mm/day were liable to trigger debris flows in the valley. The modes of deformation and failure of the landslide induced by rainstorms can be divided into three types: gully

erosion at the slope surface, shallow sliding failure, and slope foot erosion. When the rainfall intensity was greater than the soil infiltration rate, the excess water flowed away along the gullies in the landslide resulting in a progressive increase in gully size – the largest with a maximum depth of 1.7 m. For this reason, collapse occurred along the largest gully and in this case the deformation was only about 12 cm in depth. The second type of failure was controlled by the cracks which developed in the dry season. During a rainstorm, the rainfall rapidly infiltrated along these cracks, causing a rapid decrease in soil strength and thus triggering shallow sliding failure. This phenomenon often occurred in the central-upper part of the landslide at the beginning of the rainy season. During the rainy season, the loose soil was frequently disturbed by rainfall and the cracks were buried by the loose soil disturbed by the rainstorm. The third type of failure was the indirect result of rainfall. Rainstorms of magnitude >20 mm/day always triggered debris flows in the valley, and at these times the toe of the landslide was eroded and the increasing size of the free face would cause the front of the landslide to slide.

The change laws between pore-water pressure and velocity need a natural explanation by means of field monitoring. The landslide accelerated as the pore-pressure rose and decelerated as it fell. This phenomenon can be explained in the Coulomb failure (e.g., Lambe and Whitman 1969) and Newton's second law of motion:

$$ma = \tau - c(\sigma - \mu) \tan \varphi \quad (1)$$

where  $\tau$  = shear stress in the sliding zone,  $c$  = soil cohesion and  $\varphi$  = internal friction angle, respectively,  $\sigma$  = total normal stress and  $\mu$  = pore-water pressure in the sliding zone, respectively,  $m$  = landslide mass per unit area in the sliding surface, and  $a$  = landslide acceleration. The static water layer around the sliding zone controls the value of  $\mu$ , with rainfall rise resulting in increased  $\mu$ .

Form Eq.(1), a decrease of pore-water pressure ( $\mu$ ) resulted in deceleration ( $a$ ) in AB of Figure 7. The reason is that the dissipation of pore-water and soil consolidation caused the recovery of soil strength in the sliding zone. In BC, the pore-water pressure ( $\mu$ ) was negative, the soil strength continued to recover, and the landslide went into a steady-state creep stage. In CD, there was not large change in pore-water pressure (negative) and the

velocity should be same with that in BC, but it is not. The reason should be the push of from L1 to L2. In DE, an increase of pore-water pressure ( $\mu$ ) induced the loss of soil strength and resulted in acceleration ( $a$ ), the push continued to work. In EF, Eq.(1) is not established, because an acceleration ( $a$ ) and a decrease of pore-water pressure ( $\mu$ ) occurred at the same time. This can be explained by shear-induced dilation and this phenomenon has been reproduced during laboratory testing, field-scale experiments, and physically based theoretical modeling (Rudnicki 1984; Iverson et al. 2000; Moore and Iverson 2002; Schulz 2009). According to Iverson et al. (1997), the pore-water pressure change induced by shear-induced dilation can be estimated by:

$$t_{def}/t_{diff} \approx (KE)/(\gamma_w T v) \quad (2)$$

where  $t_{def}$ =time scale for deformation (in this case, dilation) of the sliding zone,  $t_{diff}$  = time scale for pore-water pressure diffusion,  $K$  = hydraulic conductivity and  $E$ = Young's modulus of the sliding zone, respectively,  $\gamma_w$  = unit weight of water,  $T$  = thickness of the landslide, and  $v$  = velocity of the landslide. If  $t_{def}/t_{diff} < 1$ , then non-equilibrium pore-water pressures should be produced by deformation of the sliding zone during displacement. Using the saturated infiltration rate  $K$  in sliding zone ( $9.2 \times 10^{-10}$  m/s), an assumed  $E$  of 5 MPa, which is typical for clay (U.S. Army Corps of Engineers 1990),  $\gamma_w = 9.78 \times 10^3$  (Lide 1991, assuming groundwater temperature of 10°C),  $T = 5$  m (the thickness of L2), and the average measured  $v$  of  $3.5 \times 10^{-7}$  m/s (30.09 mm/d, EF in Figure 7) provides  $t_{def}/t_{diff} \approx 0.3$ . The time for pore-water pressure diffusion is more than 3 times greater than that for sliding zone deformation, so an acceleration ( $a$ ) caused a decrease of pore-water pressure ( $\mu$ ) in EF of Figure 7.

Through the monitoring and analysis, this landslide had a complex deformation after rainfall. A single rainstorm event usually change the surface morphology, for example, the volume change and the average displacement of S1-S2, S3-S4 (Figure 8) were large. It happened at the beginning of the rainy season and was controlled by rainstorm and cracks. After that, the deformation of this landslide was smaller (S4-S5, S5-S6, S6-S7 in Figure 8). But there was an increasing trend of the deformation

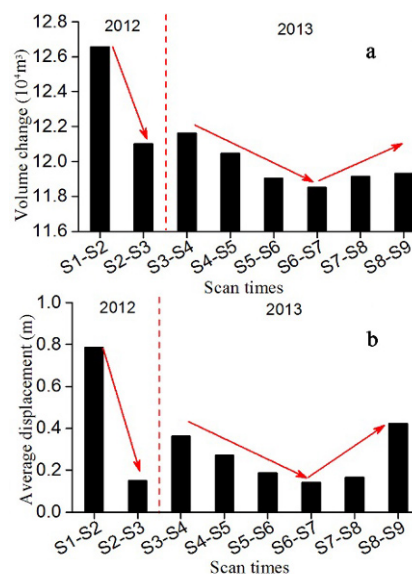


**Figure 8** The volume change (a) and the average displacement (b) of the two adjacent scanning data from TLS.

(S7-S8, S8-S9 in Figure 8) at the late of the rainy season. The main reason was not rainstorm, but a long-term rainfall infiltration. For this reason, soil was softened by water, shear strength was reduced and this landslide began to slide. It is obvious that the beginning and the late of the rainy season are two main and large deformational phases which can lead to a landslide of such magnitude that it blocks the valley.

Finally, based on the monitoring study, we conclude that ERT is well-suited to detecting changes in water content and the location of the sliding zone in the homogeneous colluvial landslides while TLS is more suited to monitoring the surface deformation of the landslide. Overall, we suggest that the combination of ERT, TLS, and traditional monitoring methods is highly appropriate for monitoring colluvial landslides.

### Acknowledgements

The research reported in this manuscript is funded by International S&T Cooperation Program of China (ISTCP) (Grant No. 2013DFE23030) and the Fundamental Research Funds for the Central Universities (Grant No. lzujbky-2014-273 and lzujbky-2015-133).

## References

- Aleotti P (2004) A warning system for rainfall-induced shallow failures. *Engineering Geology* 73(3):247-265. DOI:10.1016/j.enggeo.2004.01.007
- Anderson SA, Sitar N (1995) Analysis of rainfall-induced debris flows. *Journal of Geotechnical Engineering* 121(7):544-552. DOI: 10.1061/(ASCE)0733-9410
- Bai SB, Wang J, Lü GN, et al. (2010) GIS-based and logistic regression for landslide susceptibility mapping of Zhongxian segment in the Three Gorge area, China. *Geomorphology* 115(1):23-31. DOI:10.1016/j.geomorph.2009.09.025
- Baum RL, Johnson AM (1993) Steady movement of landslides in fine-grained soils - a model for sliding over an irregular slip surface (No. 1842). US Government Printing Office D1-D6.
- Bievre G, Jongmans D, Winiarski T, et al. (2012) Application of geophysical measurements for assessing the role of fissures in water infiltration within a clay landslide (Trièves area, French Alps). *Hydrological Processes* 26(14):2128-2142. DOI: 10.1002/hyp.7986
- Bishop AW (1960) The principles of effective stress. *TekniskUkeblad*106(39):859-863
- Burda J, Hartvich F, Valenta J, et al. (2013) Climate-induced landslide reactivation at the edge of the Most Basin (Czech Republic) – progress towards better landslide prediction. *Natural Hazards & Earth System Sciences* 13(2):361-374. DOI: 10.5194/nhess-13-361-2013
- Lambe TW, Whitman RV (1969) *Soil mechanics*. Wiley, New York.
- Morgenstern NR, Price VE (1965) The analysis of the stability of general slip surfaces. *Geotechnique* 15(1): 79-93. DOI: 10.1680/geot.1965.15.1.79
- Casula G, Mora P, Bianchi MG (2010) Detection of terrain morphologic features using GPS, TLS, and land surveys: “tanadellavolpe” blind valley case study. *Journal of Surveying Engineering* 136(3):132-138. DOI: 10.1061/(ASCE)SU.1943-5428.0000022
- Chen G (2014) Landslide susceptibility analysis in the middle reach of Bailong river basin. Doctoral dissertation, Lanzhou University. (In Chinese)
- Chen H, Lee CF (2003) A dynamic model for rainfall-induced landslides on natural slopes. *Geomorphology* 51(4):269-288. DOI: 10.1016/S0169-555X(02)00224-6
- Crozier MJ (1999) Prediction of rainfall - triggered landslides: A test of the antecedent water status model. *Earth Surface Processes & Landforms* 24(9): 825-833. DOI: 10.1002/(SICI)1096-9837(199908)
- Dai FC, Lee CF (2001) Frequency–volume relation and prediction of rainfall-induced landslides. *Engineering Geology* 59(3):253-266. DOI:10.1016/S0013-7952(00)00077-6
- Fan JL (2008) The test research on soil landslide's stability influenced by crack water. Doctoral dissertation, Chengdu University of Technology. (In Chinese)
- Giannecchini R (2006) Relationship between rainfall and shallow landslides in the southern Apuan Alps (Italy). *Natural Hazards & Earth System Sciences* 6(3):357-364.
- Guzzetti F, Peruccacci S, Rossi M, et al. (2007) Rainfall thresholds for the initiation of landslides in central and southern Europe. *Meteorology & Atmospheric Physics* 98(3-4): 239-267. DOI: 10.1007/s00703-007-0262-7
- Iverson RM, Reid ME, Iverson NR, et al. (2000) Acutesensitivity of landslide rates to initial soil porosity. *Science* 290:513-516.
- Jongmans D, Garambois S (2007) Geophysical investigation of landslides: a review. *Bulletin De La SociétéGéologique De France* 178(2):101-112. DOI: 10.2113/gssgfbull.178.2.101
- Lacerda WA (2007) Landslide initiation in saprolite and colluvium in southern Brazil: field and laboratory observations. *Geomorphology* 87(3):104-119. DOI: 10.1016/j.geomorph.2006.03.037
- Meisina C, Scarabelli S (2007) A comparative analysis of terrain stability models for predicting shallow landslides in colluvial soils. *Geomorphology* 87(3):207-223. DOI:10.1016/j.geomorph.2006.03.039
- Monserrat O, Crosetto M (2008). Deformation measurement using terrestrial laser scanning data and least squares 3D surface matching. *ISPRS Journal of Photogrammetry and Remote Sensing* 63(1):142-154. DOI: 10.1016/j.isprsjprs.2007.07.008
- Moore PL, Iverson NR (2002) Slow episodic shear of granular materials regulated by dilatant strengthening. *Geology* 30(9):843-846. DOI: 10.1130/0091-7613
- Ochiai H, Okada Y, Furuya G, et al. (2004) A fluidized landslide on a natural slope by artificial rainfall. *Landslides* 1(3):211-219. DOI: 10.1007/s10346-004-0030-4
- Park SG, Kim JH (2005) Geological survey by electrical resistivity prospecting in landslide area. *Geosystem Engineering* 8(2):35-42. DOI:10.1080/12269328.2005.10541234
- Perrone A, Lapenna V, Piscitelli S (2014) Electrical resistivity tomography technique for landslide investigation: A review. *Earth-Science Reviews* 135:65-82. DOI: 10.1016/j.earscirev.2014.04.002
- Polemio M, Sdao F (1999) The role of rainfall in the landslide hazard: the case of the Avigliano urban area (Southern Apennines, Italy). *Engineering Geology* 53(3):297-309. DOI: 10.1016/S0013-7952(98)00083-0
- Rudnicki JW (1984) Effects of dilatant hardening on the development of concentrated shear deformation in fissured rock masses. *Journal of Geophysical Research* 89(B11):9259-9270. DOI: 10.1029/JB089iB11p09259
- Satio M (1969) Forecasting time of slope failure by tertiary creep. *Proc. 7th Int. Conference on Soil Mechanics and Foundation Engineering* 2:677-683.
- Schulz WH, Mckenna JP, Kibler JD, et al. (2009) Relations between hydrology and velocity of a continuously moving landslide—evidence of pore-pressure feedback regulating landslide motion? *Landslides* 6(3):181-190. DOI:10.1007/s10346-009-0157-4
- Song H, Cui W (2015) A large-scale colluvial landslide caused by multiple factors: mechanism analysis and phased stabilization. *Landslides*13(2): 321-335. DOI: 10.1007/s10346-015-0560-y
- Teza G, Galgano A, Zaltron N, et al. (2007) Terrestrial laser scanner to detect landslide displacement fields: a new approach. *International Journal of Remote Sensing* 28:3425-3446. DOI: 10.1080/01431160601024234
- Tsaras I, Rahardjo H, Toll DG, et al. (2002) Controlling parameters for rainfall-induced landslides. *Computers and geotechnics*29(1):1-27. DOI: 10.1016/S0266-352X(01)00019-2
- Tu XB, Kwong AKL, Dai FC, et al. (2009) Field monitoring of rainfall infiltration in a loess slope and analysis of failure mechanism of rainfall-induced landslides. *Engineering Geology* 105(1):134-150. DOI: 10.1016/j.enggeo.2008.11.011
- Wang G, Philips D, Joyce J, et al. (2011) The integration of TLS and continuous GPS to study landslide deformation: a case study in Puerto Rico. *Journal of Geodetic Science* 1(1):25-34. DOI: 10.2478/v10156-010-0004-5
- Wang GL (2013) Lessons learned from protective measures associated with the 2010 Zhouqu debris flow disaster in China. *Natural Hazards* 69(3):1835-1847. DOI: 10.1007/s11069-013-0772-1
- Xu Q, Yuan Y, Zeng YP, et al. (2011) Some new pre-warning criteria for creep slope failure. *Science China Technological Sciences*54(S1):210-220. DOI: 10.1007/s11431-011-4640-5
- Yuan DY, Lei ZS, He WG, et al. (2007) Textual research of Wudu earthquake in 186 B.C. in Gansu Province, China and discussion on its causative structure. *ActaSeismologicaSinica* 20(6):696-707. DOI: 10.1007/s11589-007-0696-5